Presented at 50th European Rotorcraft Forum, Marseille, France, 10-12 September, 2024

COMPARING METHODS TO EXTRACT SECTIONAL ANGLE OF ATTACK FROM BLADE-RESOLVED ROTOR SIMULATIONS

Denis-Gabriel Caprace
Oak Ridge Assoc. Univ.
NASA Ames Research Center
Moffett Field, CA, USA

Maxim Mounier
Metis Tech. Solutions Inc.
NASA Ames Research Center
Moffett Field, CA, USA

David Garcia Perez
Science & Tech. Corp.
NASA Ames Research Center
Moffett Field, CA, USA

Patricia Ventura Diaz
Science & Tech. Corp.
NASA Ames Research Center
Moffett Field, CA, USA

Seokkwan Yoon
NASA Advanced
Supercomputing Division
NASA Ames Research Center
Moffett Field, CA, USA

ABSTRACT

The angle of attack is widely used to describe the aerodynamics of rotor blades. Models based on lifting lines, actuator lines, and actuator disks use it as a primary variable, assuming the aerodynamics can be represented by the flow around a collection of equivalent 2D airfoils. This paper evaluates the accuracy of existing methods that extract the angle of attack from blade-resolved CFD simulations, towards enabling a direct comparison of angle of attack between blade-resolved and blade-modeled simulations. Results are compared for a 2D airfoil for which the angle of attack is known by definition. The hovering rotor case is also considered, where we look at two different rotor blades. We discuss the factors that impact the accuracy of the 2D predictions. For the 3D rotors, we show that three-dimensional effects in the root and tip regions lead to large discrepancies between methods. This suggests that the very definition of angle of attack is unable to accurately represent the flow in these regions. Finally, based on guidelines that we establish, we propose an alternate method that uses local velocities sampled on a contour located 0.25 chord, or less, away from the airfoil surface and generally yields improved accuracy compared to most existing techniques.

NOTATION

a	Induction factor
c	Chord length, m
C_d	Drag coefficient
C_l	Lift coefficient
M	Mach number
r	Blade radial coordinate, m
R	Blade radius, m
Re	Reynolds number
u	Local velocity, $\mathrm{m\,s^{-1}}$
u_e	Effective Velocity, $\mathrm{m\,s^{-1}}$
α	Angle of attack, $^\circ$
α_{ref}	Reference angle of attack, $^\circ$
γ	Circulation per unit length, $\mathrm{m\,s^{-1}}$
Γ	Circulation, $\mathrm{m^2\,s^{-1}}$
θ_0	Collective pitch angle, $^\circ$
Ω	Closed contour around the airfoil

INTRODUCTION

Engineers commonly refer to the angle of attack (AoA) of aerodynamic profiles when describing their aerodynamics. It is generally understood as the angle between an effective flow velocity vector and the longitudinal axis of the profiles, usually their chord. Although often very useful in providing insight into the relation between local flow conditions and measured or computed forces and moments, the AoA technically derives from an arbitrary definition that is only valid in two dimensions. In complex three-dimensional configurations such as the flow induced by a rotorcraft, the AoA is not well defined. This paper reviews and compares existing post-processing methods to extract the angle of attack from computational fluid dynamics (CFD) results, with a particular focus on rotorcraft applications. A new method is also introduced to improve on existing algorithms.

In addition to its value as an intuitive metric, the AoA has a key role in several aerodynamic simulation techniques

whereby the geometry is modeled. For instance, blade element momentum theory, lifting line, and actuator methods employ AoA as a primary internal variable. These methods rely on external 2D airfoil tables (a.k.a. polars) to relate locally sampled AoA and blade forces. On the other hand, geometry-accurate data resulting from 3D experiments or blade-resolved simulations are independent of the definition of an angle of attack. To reconcile geometry-modeled and geometry-accurate approaches, it is desirable to (1) utilize a self-consistent technique to sample the AoA from the flow in the former; (2) dispose of a self-consistent method to extract the angle of attack from the latter. Self-consistency here refers to a method that outputs the correct angle of attack in a reference case where it is geometrically known and well-defined (i.e., in a benchmark 2D setup).

The first point has been the focus of continuous efforts over the last decade. The Actuator Disk (AD) and Actuator Line Model (ALM) have been popular in the wind energy community since their inception, see reviews in (Refs. 1, 2). Several variations have been proposed over the years to adapt how the effective velocity is sampled in the simulation, a testimony to the inherently ambiguous character of the AoA. For AD methods, a version based on effective velocity (Ref. 3) that is different from the velocity at the disk (Ref. 4) has been proposed. For ALM, it is theoretically preferable to use an integral velocity sampling to maintain the consistency of the inherent smoothing approach, stemming from a mathematical argument (Ref. 5). Nevertheless, different sampling techniques have been introduced, including pointwise and integral velocity samplings (Refs. 6,7), correction for local drag (Refs. 8,9), Lagrangian sampling (Ref. 10), and other sampling distributions (Refs. 11,12). Interestingly, the latter references employ a line average technique initially proposed for AoA extraction of geometry-resolving simulations (as detailed below). In the rotorcraft community, while lifting line approaches have been used extensively in free-wake methods (Ref. 13), actuator methods have recently gained popularity, both in their disk (Refs. 14–16) and line formulations (Refs. 17–20).

Regarding the second point, existing methods to determine the AoA from geometry-accurate data can be subdivided into three categories: methods based on axial induction (Refs. 21, 22), methods based on surface pressure (Refs. 23, 24), and methods based on flow velocities (Refs. 25–29). Previous works have compared a variety of these methods and assessed their effectiveness for horizontal axis wind turbines (Refs. 30, 31). The scope of comparisons was recently extended to vertical axis wind turbines (Refs. 32,33).

However, the usability of such AoA extraction methods has never been evaluated for rotorcraft applications. A notable difference between helicopter rotors in hover and wind turbines is the prevalence of perpendicular blade vortex interactions. As opposed to wind turbines that always operate under a non-zero inflow, the preceding tip vortex of a rotorcraft in hover stays closer to the blade. In forward flight, parallel and perpendicular blade vortex interactions (BVIs) are also generally experienced. The presence of a vortex in the vicinity of a section of interest affects the result of the AoA extraction in a way that needs to be quantified.

In this paper, we first describe the procedure behind a list of existing AoA extraction methods. We also introduce an alternate procedure of our own. We then compare the extraction results in a 2D configuration that allows us to conclude on the extraction error of each method. Finally, we evaluate the performance of each extraction method in a 3D configuration simulating two different rotors in hover, and we highlight the difficulties arising from the presence of the preceding tip vortex. We conclude with recommendations on AoA extraction for rotorcraft applications.

AOA EXTRACTION METHODS

To favor their usability in the most general case, we are mostly interested in standalone methods allowing for AoA extraction based solely on the gathered geometry-accurate data, and that are applicable to any configuration, such as wings, rotors, etc, and arbitrary inflow orientations. Pressure-based methods rely on external 2D polar data to connect computed forces to angle of attack, which makes them dependent on the availability of such 2D polar data. Similarly, induction-based methods are only applicable to rotors in axial flow conditions, owing to the tangential averaging employed to obtain the mean axial and swirl induction. Therefore, we limit our scope to velocity-based methods that do not require any external inputs and are not limited to specific rotor configurations. For the sake of performing comparisons, we still include one pressure-based procedure. We also focus on blade-resolved CFD simulations rather than experiments, as it is easier to probe local velocities in a non-intrusive manner in the former.

The following sections provide a brief description of six velocity-based AoA extraction techniques. They have in common that they aim to extract an effective velocity, that is, a velocity insensitive to the effect of the local airfoil circulation while still being affected by all other sources of vorticity in the flow, such as other blades, vortices, etc. All methods work in a 2D plane that contains the local airfoil section. In the 3D case, when flow-sampled velocities are needed, they are always projected into this plane before any calculation is performed. The AoA is defined as the angle between the airfoil chord, c, and this effective velocity, u_e,

$$\alpha = \angle(\mathbf{c}, \mathbf{u}_e). \tag{1}$$

For simplicity, the procedures are described for the case of an immobile airfoil in the frame used to express the velocity. They can be easily extended to the hovering rotor case by subtracting the local blade rotational velocity from the effective velocity before computing the angle with the chord.

The following sections provide a brief summary of each selected method. For more details on their foundations, we refer the reader to the original publications.

Shen et al. (Ref. 25)

Shen et al.'s method (hereafter referred to as Shen 1) consists in deriving the effective velocity by directly subtracting self-

induction from the velocity sampled at an arbitrary monitoring point located in front of the blade in the rotor plane, as shown in Fig. 1. The bound vorticity is represented as a singular point vortex located at the quarter chord, and its influence on the sampling point is evaluated using the Biot–Savart law. The circulation around the airfoil is computed by integrating the circulation per unit length of the boundary layer over the airfoil surface. For this purpose, the total velocity deficit across the boundary layer is calculated using the pressure at the wall (measured in the experiment or computed in the blade resolved simulation) and Bernoulli's principle.

Figure 1: Sketch of the Shen 1 method with one sampling point in front of the airfoil (•). The circulation is computed using the pressure on the airfoil surface (—) and assumed concentrated at the quarter chord (•) when evaluating its influence.

Shen et al. (Ref. 26)

The same authors proposed an alternate technique (hereafter referred to as Shen 2) to address the deteriorated performance of the original method when the sampling point is close to the airfoil. This alternate technique is better suited for use when it is difficult to get experimental data far away from the airfoil. The extraction procedure follows the same steps except for the assumption that the circulation is concentrated in a point vortex located at the quarter chord. Instead, the bound circulation is assumed to be distributed on the airfoil surface (Fig. 2) with a circulation per unit length proportional to the delta velocity obtained from the steady Bernoulli equation. Since the circulation distribution now reflects the airfoil geometry, one can use a sampling point closer to the blade, e.g., between $0.5c$ and $2.0c$.

Figure 2: Sketch of the Shen 2 method with one sampling point in front of the airfoil (•). The circulation is computed using the pressure on the airfoil surface (—) and locally redistributed along the airfoil surface (- -) when evaluating its influence.

Line average method (Ref. 27)

The line average method computes the effective velocity as:

$$\mathbf{u}_\mathrm{e} = \frac{1}{L}\int_\Omega \mathbf{u}\,\mathrm{d}\ell \approx \sum_{j=1}^{N} \mathbf{u}_j \frac{\Delta_j}{L}, \tag{2}$$

where L is the length of a closed contour Ω around the airfoil (Fig. 3), $\mathbf{u}$ is the local velocity, and the contour is discretized in N panels.

This expression implicitly assumes that all the airfoil bound vorticity is concentrated in a point located at the geometric center of the contour. The contour needs to be symmetric with respect to point reflection at its center. Hence, by construction, the integral of the velocity over the contour cancels out the contribution of the bound vorticity. Therefore, the circulation does not need to be computed explicitly.

Due to the assumption of concentrated point vorticity, the approach is expected to work only for contours relatively far away from the airfoil surface. Typically, the recommended value is a contour of radius equal to one chord length.

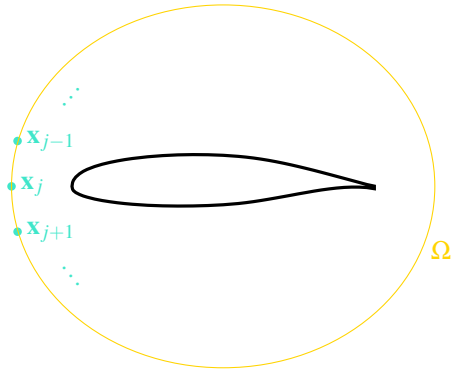

Figure 3: Sketch of the line average method that samples velocity on a contour Ω (—) with discretized points (•). The circulation is not explicitly computed.

Rahimi et al. (Ref. 28)

Rahimi et al.'s method (Ref. 30) uses three points along the chord length on each side of an airfoil section (Fig. 4), recommended to be at a distance around one chord length from the airfoil. It is assumed that a symmetric placement of the sampling points eliminates the influence of bound-circulation-induced velocity. The method extracts the effective velocity by first averaging the velocity between each pair of points on the suction and pressure side locations, leading to three averaged velocities spread along the chord-wise direction at 25, 50 and 75% of the chord. An additional average of these three velocities is performed and yields the effective velocity. Similar to the line average method, the airfoil circulation is neither computed nor explicitly corrected for.

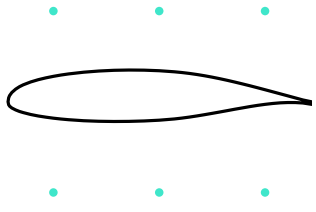

Figure 4: Sketch of the Rahimi method that samples velocity at six points in the suction and pressure side regions (•). The circulation is not explicitly computed.

Zhong et al. (Ref. 29)

Zhong et al.'s procedure is illustrated in Fig. 5 and works as follows: (1) determine the circulation distribution on the airfoil using the same method as Shen et al. (Ref. 26); (2) select two sampling points close to the aerodynamic center on both pressure and suction sides. The authors do not give guidelines regarding their minimum distance to the wall, but they note that they can be adjacent to the airfoil. (3) Subtract the airfoil self-induction from the velocity at each sampling point using a procedure similar to Shen 2; (4) average the velocity of the two monitoring points obtained in Step 3 to obtain the effective velocity.

The authors report a relative error on the induced velocity magnitude of less than 5%.

Figure 5: Sketch of the Zhong method with two sampling points adjacent to the airfoil suction and pressure side at the quarter chord location (•). The circulation is computed using the pressure on the airfoil surface (—) and locally redistributed along the airfoil surface (- -) when evaluating its influence.

Caprace et al. (present work)

We introduce a new method as an attempt to overcome some of the limitations of existing techniques, particularly in rotorcraft applications. In this context, it is desirable to work with sampling points relatively close to the airfoil (ideally less than $0.5c$ away) to minimize the influence of preceding tip vortices. Also, we aim to relax the geometric constraint of symmetry on the sampling points as we would like to use information on native CFD grids without the need for additional interpolation. Nevertheless, we keep a structure similar to the other procedures.

Caprace et al.'s AoA extraction scheme involves four steps, sketched in Fig. 6: (1) compute the circulation Γ using its definition as a contour integral:

$$\Gamma = \int_\Omega (\mathbf{u}\cdot\hat{\mathbf{t}})\,\mathrm{d}\ell \approx \sum_{j=1}^{N} (\mathbf{u}_j\cdot\hat{\mathbf{t}}_j)\Delta_j, \tag{3}$$

where Ω is a closed contour around the airfoil, $\hat{\mathbf{t}}$ is its tangent vector, and we discretize the contour in N panels, e.g., using the available body-fitted grid; (2) for each point along the same contour, compute an estimate of the velocity induced by the bound circulation $\mathbf{u}_{\Gamma_j}$ using the Biot-Savart law. The circulation of the airfoil is assumed to be distributed on the airfoil surface. However, instead of using pressure information and Bernoulli's principle, we assume that the circulation per unit length γ along the contour only depends on the chordwise location and scales with:

$$\gamma \sim \frac{c-x}{x}, \tag{4}$$

where x is the chordwise coordinate. (3) Compute the effective velocity as:

$$\mathbf{u}_\mathrm{e} = \frac{1}{L}\int_\Omega (\mathbf{u}-\mathbf{u}_\Gamma)\,\mathrm{d}\ell \approx \sum_{j=1}^{N} (\mathbf{u}_j - \mathbf{u}_{\Gamma_j})\frac{\Delta_j}{L}. \tag{5}$$

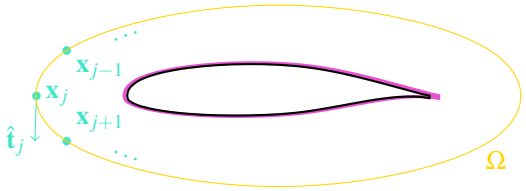

Figure 6: Sketch of the Caprace method that samples velocity on a contour Ω (—) with discretized points (•). The circulation is computed using an integral of the velocity along the same contour and locally redistributed along the airfoil surface (- -) when evaluating its influence.

Inverse blade-element momentum (BEM)

When airfoil data is available by independent means, it is possible to estimate α using the loads computed in the blade-resolved simulation. In that case, the flow information is not used. The procedure, as proposed by various authors, is termed inverse BEM, as it backtracks α from the airfoil starting from the loads, whereas the BEM instead calculates the loads for a given angle of attack.

An iterative technique is needed as one must determine both the direction and the magnitude of the effective velocity vector in the plane of each airfoil section on the blade. Ideally, one should rely on 2D aerodynamic lift and drag coefficients for the airfoil, tabulated as a function of angle of attack, Reynolds number, and Mach number. As this information may not be available, interpolation between existing data points can be used, although this very likely deteriorates the accuracy of the angle of attack extraction.

The procedure implemented in the current study is similar to that proposed by Lindenburg (Ref. 34), except that we neglect tangential induction. It works with the normal force coefficient as the main variable, where the normal force computed in the simulation is f_n. For each radial station along the blade, we start with an initial guess of the induction factor $a = \frac{u}{r\Omega}$. The following steps are then taken: (1) compute the effective velocity magnitude $u_\mathrm{e} = r\Omega\sqrt{1+a^2}$; (2) compute the corresponding Reynolds and Mach numbers; (3) interpolate the lift and drag coefficients, C_l, C_d for Re and M at hand; (4) solve for α the expression

$$\frac{1}{2}\rho u_\mathrm{e}^2 c\,(\cos(\alpha)C_l(\alpha) + \sin(\alpha)C_d(\alpha)) = f_n;$$

(5) calculate the new induction factor $a = \tan(\alpha+\theta)$ where θ is the local twist angle; (6) return to (1) until convergence is reached for the induction factor a.

It is common for methods using 2D airfoil data to apply additional corrections to the lift and drag coefficients to account

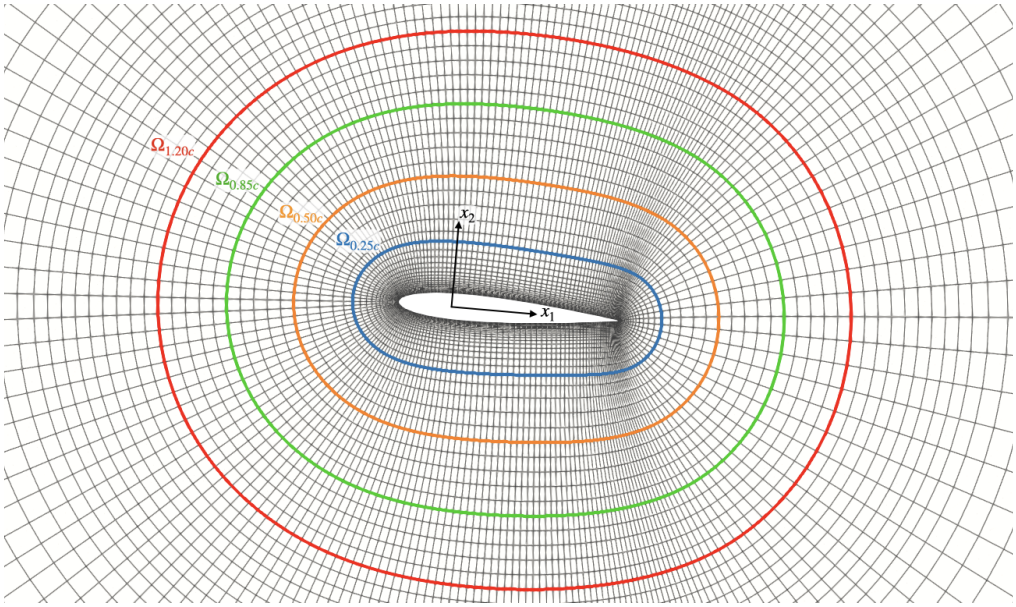

Figure 7: Mesh of a NACA0012 used for the 2D airfoil simulations, with probing contour $\Omega_{0.25c}$ at an average distance of 0.25 chord from the surface, $\Omega_{0.50c}$ at 0.5 chord, $\Omega_{0.85c}$ at 0.85 chord, and $\Omega_{1.20c}$ at 1.2 chord.

for compressibility effects, Reynolds number effects, and rotational effects (in the blade root region). In the present work, we rely on the usual Prandtl-Glauert correction for Mach effects, a power law for Reynolds effect (Ref. 35), and the Du and Selig (Ref. 36) rotational correction, respectively.

RESULTS AND COMPARISONS

Numerical Setup

NASA's OVERFLOW solver (Ref. 37) is utilized to obtain a prediction of the flow field on airfoils and rotors. OVERFLOW is a finite-difference CFD code that solves the Reynolds-averaged Navier-Stokes equations in conservation form and offers several inviscid flux algorithms, implicit numerical schemes, and turbulence models. The results presented in this paper all take advantage of the delayed detached eddy simulation mode where the Spalart-Allmaras turbulence model is used in the vicinity of the wall. Inviscid fluxes are discretized using the sixth-order accurate central difference scheme with fifth-order artificial dissipation. The viscous terms are discretized to second order. The simulations are advanced in time using the second-order backward differentiation formula. Dual time-stepping is used with a constant CFL number of 1. The inner loop is converged until a drop of three orders of magnitude in sub-iteration residual is attained or 50 subiterations are reached, whichever comes first.

For the 2D airfoil simulations, we consider the NACA 0012 airfoil geometry. A single O-mesh is built around the surface geometry with points distributed along the surface curvilinear coordinate, as seen in Figure 7. The grid points are clustered in the leading and trailing edge regions. The volume grids are grown from the surface up to a distance of 100 chord lengths using a hyperbolic technique. The distance of the first grid point to the wall is chosen to satisfy the $y^+ < 1$ condition in the simulation.

For the 3D rotor simulations, we consider two rotor geometries. The first rotor geometry examined is a full-scale model of the XV-15 rotor, which features a highly-twisted three-bladed design with airfoils of the NACA 64-series, and has been the subject of various tiltrotor research activities (Ref. 38). The rotor solidity is 0.089. Simulations are conducted at a nominal tip Mach number of 0.69. The second rotor geometry considered is that of a canonical quadrotor urban air taxi (Ref. 39), featuring a three-bladed rotor with low twist and modern VR12/SSCA09 airfoils along the span. The rotor solidity is 0.0647. It is operated at a nominal tip Mach number of 0.5. The results presented here were obtained with the exact same rotor grids utilized in our previous publications (Ref. 39, 40), and we refer the reader to them for additional details on the grid generation process using the overset grid methodology. Essentially, three body-conforming grids are used to resolve the flow in the vicinity of the blades, including an O-grid for the main surface of the blade and two cap grids for the root and tip. Similarly, three grids of the same topology are used for the hub's main surface and singular axes. Grid point distribution is densely clustered near the leading and trailing edges in the chordwise direction and near the root and tip in the spanwise direction. Grid spacing near the wall satisfies the $y^+ < 1$ criterion to achieve adequate boundary layer resolution. A Cartesian off-body grid uniformly spaced at $10\,\%\,c_{\text{tip}}$ is used to resolve the rotor wake. Additional levels of refinement, each twice as coarse as the preceding level, efficiently expand the computational domain to the far field, located 20 radii away from the center of the rotors in all directions.

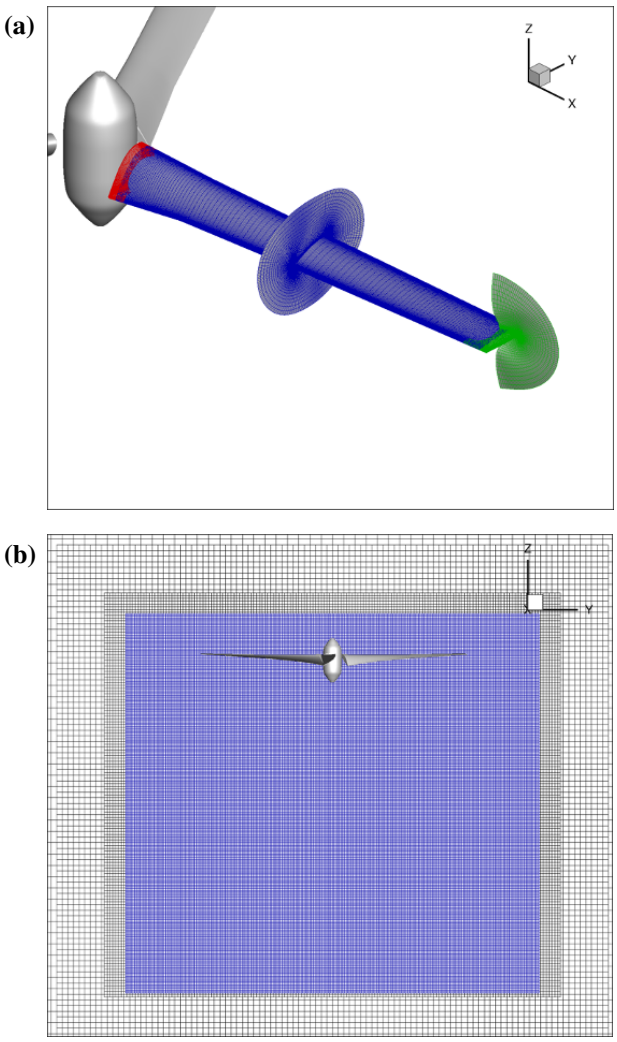

Figure 8: Overset grid system for an isolated XV-15 rotor: (a) rotating near-body curvilinear grids and (b) fixed off-body Cartesian grids.

Figure 8 shows the overset grid system generated for the XV-15 rotor. Figure 9 shows the overset grid system generated for the quadrotor urban air taxi rotor.

Application to a 2D Airfoil

The AoA is a 2D construct that derives from how airfoil tables are measured in an experimental setup. In such a controlled environment, the inflow velocity (direction and magnitude) is known since it is a controlled parameter of the experiment. Therefore, α is defined unambiguously as the angle between the inflow velocity and the airfoil chord.

Mimicking experiments, we compare the performance of each method introduced in the previous section based on a set of 2D simulations where the reference value of the AoA (α_{ref}) is known by definition. These α_{ref} values are: 2.5°, 5°, 7.5° and 10° respectively. These reference values enable the computation of the error committed by each method, which facilitates their comparison. The NACA 0012 airfoil geometry is employed for this purpose, where our grid has 201 points along

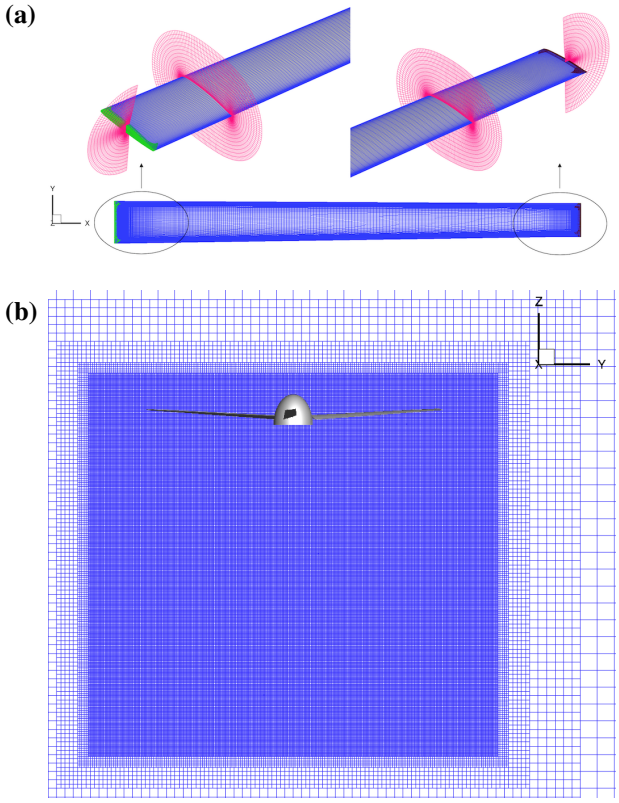

Figure 9: Overset grid system for a canonical quadrotor urban air taxi rotor: (a) rotating near-body curvilinear grids and (b) fixed off-body Cartesian grids.

the surface curvilinear coordinate.

Results are obtained for a Mach number of 0.5 and a Reynolds number of 2.6×10^6, for a range of AoAs. We compare the output of the previously introduced algorithms in Fig. 10. For each algorithm, the sampling points are positioned within the recommended distance from the airfoil, namely $1.5c$ for Shen 1 and Shen 2, $0.85c$ for the line average, $1.2c$ for Rahimi and Caprace, and the closest to adjacent of $0.25c$ for Zhong's. The accuracy of a method is determined by its error relative to the known reference values α_{ref} defined earlier. It can be seen that Zhong's method is generally the least accurate, followed by Rahimi's, both suffering from a greater than 10% error on most α_{ref}'s. They are followed by Shen 2 and Shen 1, respectively. Both Shen's and Zhong's methods exhibit an error that strongly depends on α_{ref} itself. This is due, in part, to the limited number of sampling points (respectively one or two), which makes the methods more sensitive to the local correction for self-induced velocity. This error is further amplified past stall, i.e., for $\alpha_{\text{ref}} > 9°$. On the other hand, for the methods that use more sampling points —6 for Rahimi, 201 for the line average and ours—, the error on the extracted α is almost independent of α_{ref}.

Our method outperforms the line average despite using a contour that is closer to the airfoil, which is desirable to minimize the influence of preceding tip vortices, apparent in the 3D hovering rotor cases described in the next section. This reduced dependence on contour size can be attributed to the fact that

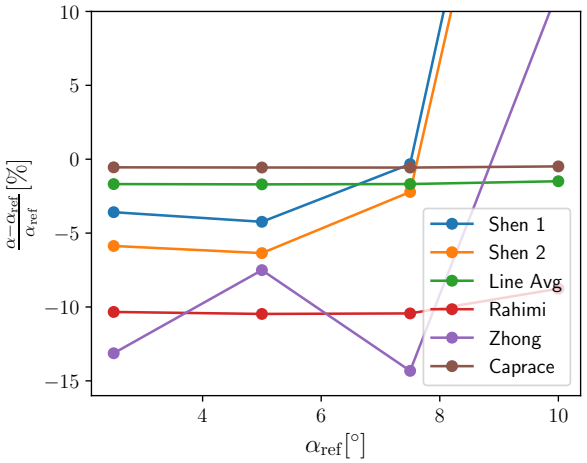

Figure 10: Relative error of the extracted AoA with respect to the reference AoA, using the recommended contour distances specified in 2D results.

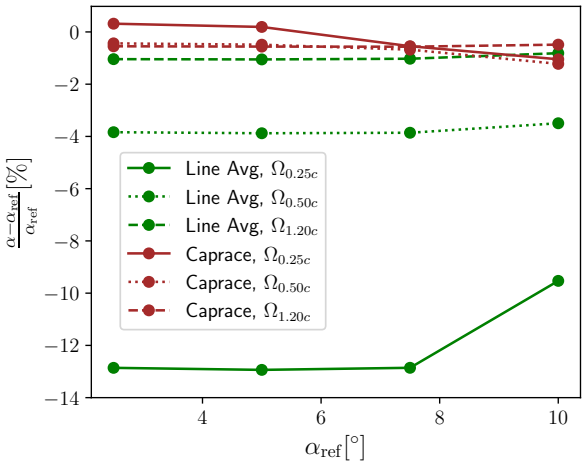

Figure 11: Relative error of the extracted AoA with respect to the geometric AoA for the line average (Ref. 27) and Caprace methods and contours of various sizes.

we explicitly correct for the airfoil self-induction whereas the line average method doesn't. The assumption made by the line average method is that the self-induction cancels out when the sampled velocity is averaged over Ω. However, this only holds if the bound circulation is concentrated at the center of the contour.

To further illustrate the effect of the chosen contour, Fig. 11 shows results obtained with the Caprace and line average methods for various sizes of the contour used to sample the local flow velocity (shown in Fig. 7). Generally, the larger the contour, the more accurate the results are for both line average and Caprace. However, Caprace's method shows a much lower sensitivity to the contour used, and outperforms the line average method for any chosen contour distance. One can also see that, for the two methods, the closest contour is more sensitive to the airfoil stalling. This is likely due to the associated change in vorticity distribution in the (separated) boundary layer around the airfoil, which departs from the distribution assumed in the model.

Although large contours provide more accurate extracted AoAs in 2D, increasing their size comes with the risk of including extraneous vorticity from other sources in the 3D contours. Such vorticity from closeby vortices (e.g., as in the case of a BVI) is unaccounted for in the models and deteriorates their accuracy. For this reason, contours closer to the airfoil should be preferred. In the end, the optimal accuracy for each extraction method requires balancing both of these effects.

Since all the aforementioned AoA extraction methods first calculate an effective velocity, one can also examine the error on its magnitude. This is relevant to blade-modeled simulations as they usually require this quantity to transform aerodynamic coefficients into their dimensional counterparts. Figure 12 shows that the magnitude is generally predicted within 1% of error for all methods except Zhong's, which has an error around 2% before shooting up to 4% when $\alpha_{\text{ref}} = 10°$, and uses sampling points very close to the airfoil surface.

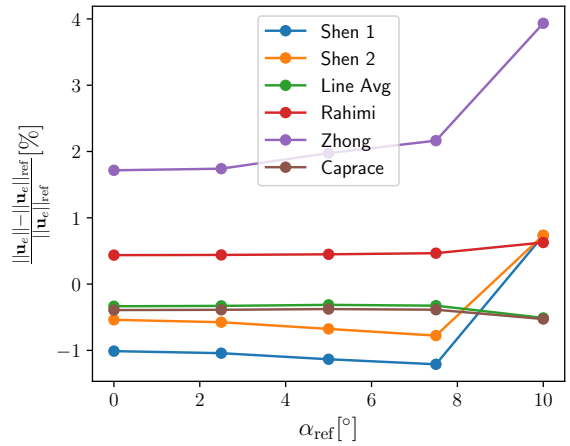

Figure 12: Relative error of the effective velocity magnitude with respect to the geometric α, using the recommended contour distances specified in 2D results.

Application to Hovering Rotors

We first consider the results obtained on the XV-15 rotor geometry. Figure 13 depicts instantaneous AoA extracted from the XV-15 rotor in hover at 3° and 10° blade pitch collective angle. We compare the performance of all the methods introduced previously, where we use a contour at an average distance of $0.61c$ from the airfoil for all methods except Zhong. The latter uses points at $0.18c$ from the airfoil surface.

We apply each method to the 121 discrete airfoil sections along the XV-15 rotor span, with each airfoil grid containing 263 points distributed along the surface curvilinear coordinate to compose a 3D result. For a hovering rotor, the inflow at each section is more complex than in purely 2D cases where the upstream velocity is uniform and known. In 3D, one needs to consider the rotor rotational speed, while external perturbations such as BVIs and spanwise flow can also

arise. Because there is no analytic reference for α, it is impossible to compute an error. Nevertheless, third-party results are here obtained from the inverse BEM method. Since the latter determines α from the loads computed in the blade-resolved simulation, these results are truly independent of the flow information, and therefore, of the other AoA extraction algorithms. Therefore, the inverse BEM results are used to control their consistency.

We observe that Zhong's method is generally the least accurate and completely misses the variation of α along the blade span, likely due to the sampling points being too close to the airfoil surface for the self-induction correction to be accurate. Compared to Zhong's method, Rahimi's performs better along the midsection of the rotor blade, however still featuring a larger discrepancy with the inverse BEM results.

Shen 1 and Shen 2 agree the most favorably with the inverse BEM, but the agreement deteriorates heavily toward the root, most likely due to local three-dimensional effects. The line average and Caprace's methods yield similar results at mid span and blade tip, but Caprace's is slightly better near the root section because it uses a closer contour and corrects for self-induction. Nevertheless, three dimensional effects are still affecting the agreement.

In the tip region at $\theta_0 = 10^\circ$, the influence of the preceding vortex is clearly seen with a relatively sharp increase in α at around $r/R = 0.9$ for all velocity-based extraction methods. The inverse BEM also exhibits an increase, albeit about four times smaller. The blade vortex interaction with the preceding tip vortex results in a locally three-dimensional flow, which breaks the assumption made in both velocity-based and load-based extraction methods that the flow remains 2D. These methods are bound to fail in those regions unless a proper 3D correction is developed.

In the tip region at $\theta_0 = 3^\circ$, the influence of the preceding vortex is less noticeable than in the $\theta_0 = 10^\circ$ case since the tip vortex circulation is smaller, but we still see an increase of α at around $r/R = 0.9$ for all velocity-based extraction methods. We can also notice that the jumps are exaggerated for methods that sample fewer points. For example, the Shen 1 and Shen 2 methods that sample a single point in front of the leading edge have a significant dip in α at around $r/R = 0.8$ and then increase past the others at $r/R = 0.9$. For Zhong's method, where two points are sampled, and Rahimi's, where six points are sampled, we have a similar magnitude jump in α at around $r/R = 0.8$. For line average and Caprace's methods, which sample the 263 points of the grid, we have the smallest magnitude discrepancy. The effects of complex 3D flow features near the tip are smoothed out with methods that sample more points due to the effect of spatial averaging. However, 3D effects still constitute a violation of the assumptions made in all methods, including the inverse BEM.

An additional complexity of the inverse BEM method is its sensitivity to airfoil data. For the XV-15 rotor, the airfoil data we use here was obtained from wind tunnel tests at a Reynolds over Mach ratio different than the one the rotor operates at. Despite the use of a correction for Reynolds effects, this difference adds uncertainty to the AoA extracted with the inverse BEM. For this reason, we analyze the results on a second rotor with a different set of airfoils.

The remainder of this section exposes the results obtained for the quadrotor vehicle geometry. Figure 14 depicts the AoA extracted from its isolated rotor in hover, with each rotor blade discretized in 287 sections along the span and 201 points distributed along the airfoil curvilinear coordinate. The distance between the sampling points and the airfoil surface follows the recommended value for each method, which is an adjacent one for Zhong ($0.05c$), and $0.85c$ for the other methods. Zhong's method has the least accurate α predictions, as the model of the correction for self-induction is not effective at such a close contour distance. The other methods have a favorable agreement along the midspan sections, with Rahimi having the largest discrepancy, with a largest deviation of around 1°. The others perform similarly in the midspan region, staying within a range of less than $\pm 0.5^\circ$. All these methods experience a sharp increase in α, similar to the XV-15 cases, toward the tip due to the influence of the preceding tip vortex (among other 3D effects). Shen 1 and 2 start to deviate at around $r/R = 0.75$, whereas Caprace, Rahimi, and the line average methods start to deviate at around $r/R = 0.85$. Once again, to account for the complex 3D nature of the flow in the tip region, a correction should be developed. Flow sampling as performed here is not sufficient.

Thanks to the quality of the tabulated data available for this airfoil, we note that the agreement between all velocity-based methods and the inverse BEM method is outstanding, except at the blade root and the tip. At the root, a spike in α is caused by the rotor geometry that features a gap between the hub and the blade root cutout. The gap is larger on this rotor than on the XV-15 grid, allowing some flow to traverse the rotor plane upwards, which spuriously increases α. Additionally, Jost et al. (Ref. 27) mention that near the blade root, the monitoring point locations for the Shen methods might be closer to the preceding blade than to the evaluated blade, where we notice that they perform the worst compared to other methods, regardless of the contour size used.

One can examine Fig. 15 to assess the impact of using sampling points closer to the airfoil at an average distance of $0.05c$ for each velocity-based method. This close distance is outside of the recommended bounds for all methods but Zhong's (with unchanged sampling points) and Caprace's. A closer distance reduces the amount of extraneous vorticity included in the contour. It is thus less likely for surrounding vortices to deteriorate the accuracy of the AoA extraction, which is especially relevant in the tip region. On the other hand, a too close set of sampling points risks excluding boundary layer vorticity that contributes to the total bound circulation, and possibly violates other assumptions made in each method. The figure shows that Shen 1 and Shen 2 are the most impacted when bringing the sampling points closer. Rahimi and the line average methods under-predict α by around 3° to 4° for the entire blade. Caprace's method is mostly unaffected in the mid-span

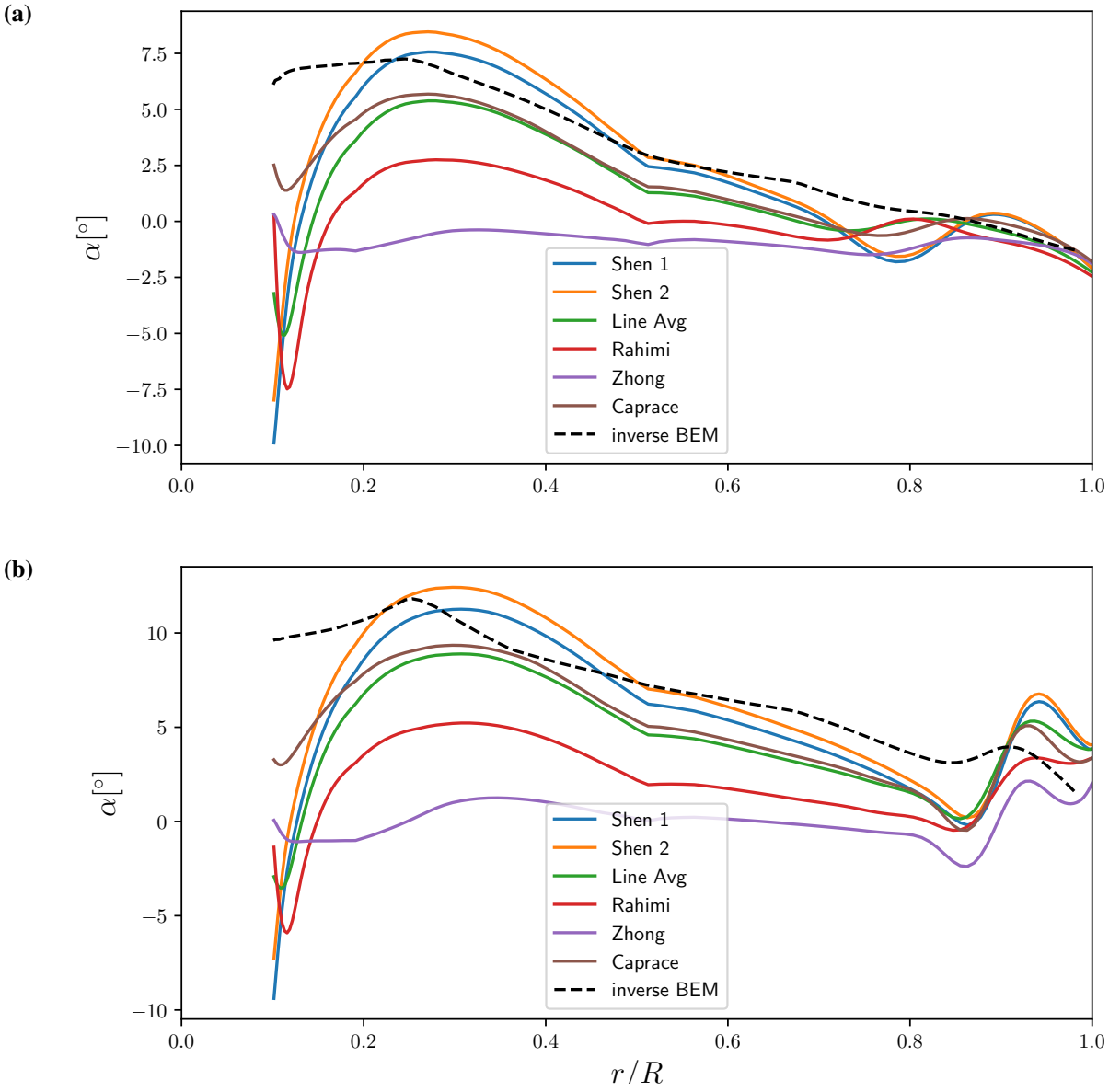

Figure 13: Radial distribution of instantaneous AoA extracted from the 3D simulation of a hovering XV-15 rotor using a contour distance of $0.61c$ for all methods except Zhong using $0.18c$, at a collective pitch angle of (a) $\theta_0 = 3°$ and (b) $\theta_0 = 10°$.

region (compared to larger contours, as already noticed from 2D results). In the tip region, the jump in α has a smaller amplitude than previously observed, bringing the extracted value closer to the inverse BEM result. This also suggests that the effect of the preceding tip vortex on the extraction is to virtually increase α when a too large contour is utilized.

CONCLUSION AND DISCUSSION

This study compared various AoA extraction methods. In 2D, we showed that their accuracy depend on where the flow velocity is sampled and what type of correction is applied to isolate the airfoil self-induction. In 3D, while no analytical solution exists, the comparison of velocity-based and load-based AoA extraction results showed that inconsistencies are amplified in the blade root and tip regions, due to three dimensional effects and the sensitivity of the load-based results to available airfoil tables. Our analysis allows us to formulate recommendations for rotorcraft applications:

- The contour used to sample the velocity should be as close as possible to the airfoil to avoid perturbation by nearby vortices. However, the contour should enclose the airfoil's boundary layer to correctly capture its circulation.
- A correction of the locally sampled velocity should be used. This correction should account for the fact that the circulation is distributed along the airfoil surface.
- The effective velocity should be obtained as an average

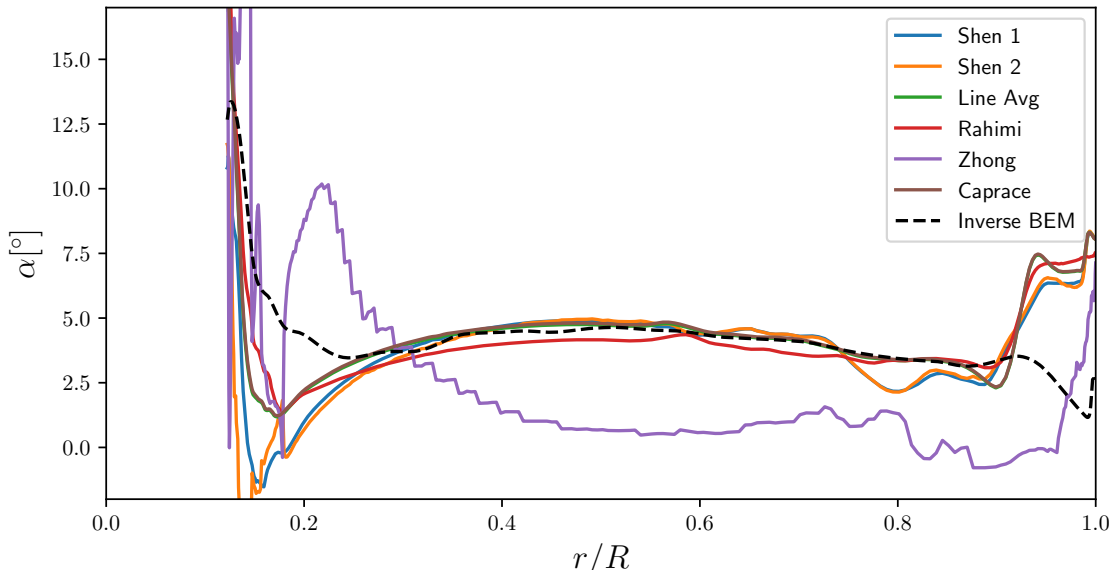

Figure 14: Radial distribution of instantaneous AoA extracted from the 3D simulation of a hovering quadrotor vehicle using a contour distance of $0.05c$ for Zhong and $0.62c$ for all other methods at a collective pitch angle of $\theta_0 = 11.5°$.

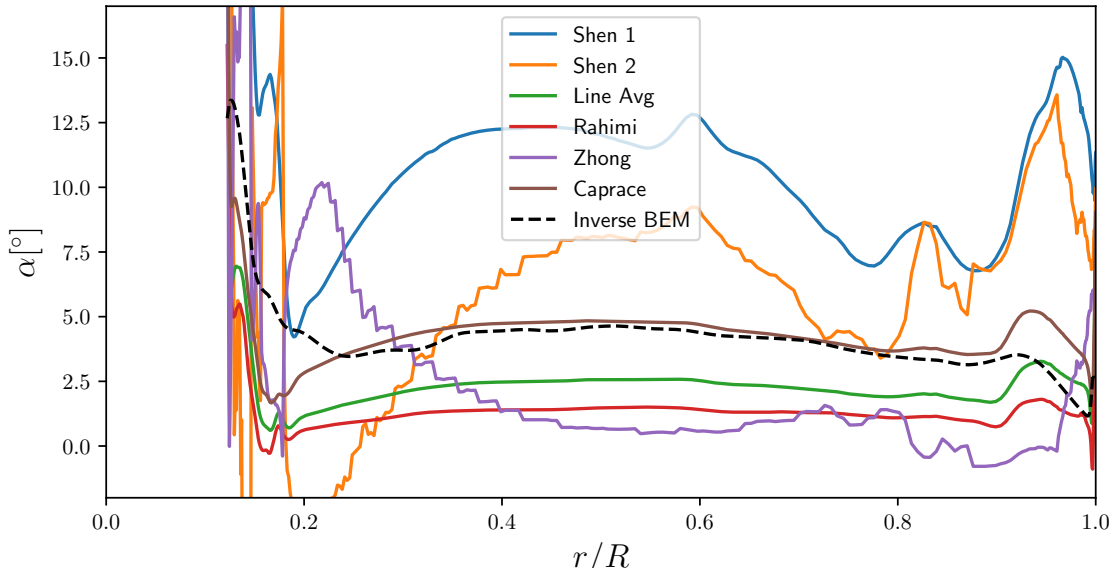

Figure 15: Radial distribution of instantaneous AoA extracted from the 3D simulation of a hovering quadrotor vehicle using all methods at the closest contour distance of $0.05c$ at a collective pitch angle of $\theta_0 = 11.5°$.

of the local velocity sampled at multiple locations (ideally, on the order of 10 to 100) around the airfoil to reduce the sensitivity of the extracted AoA to local, fine flow structures, and the correction technique.

In this work, we presented our best attempt at the implementation of the other authors' methods. It is worth noting we may have misinterpreted their work, leading to worse AoA predictions. Nevertheless, we notice that Caprace's method manages to reduce the sensitivity of the extracted AoA to the distance between the airfoil surface and the contour used for velocity integration —with working values down to $0.05c$, whereas most methods recommend $1.0c$— while simultaneously reducing the error. In addition to reducing the likelihood of including vorticity from other sources than the bound vortex, using a contour closer to the blade is expected to improve the accuracy of the extraction in the root region (Ref. 41).

Some velocity-based AoA extraction methods rely on pres-

sure information and Bernoulli's equation to determine the airfoil circulation. One way to improve their results specifically for rotorcrafts (and large scale wind turbines, too), where flow velocities exceed the incompressible regime, is using a compressibility correction as we did in this work.

On the other hand, the results for load-based methods like the inverse BEM depend on the quality of the airfoil tables used. Although corrections for compressibility effects, Reynolds number effects, and rotational effects can improve the method's performance, we stress that it is most desirable to exploit dedicated data obtained at the correct Reynolds and Mach numbers, specifically in the root and tip regions.

Regarding the consistency between blade-resolved and blade-modeled simulations, Melani et al. (Ref. 42) recently examined the capability of the ALM to resolve blade tip effects. Even with extremely high grid resolution in the region of the bound vortex to capture a Gaussian kernel with a size of about 10% of the airfoil chord, they observed disagreements of their ALM results compared to blade-resolved simulations in the tip region. Just as in the case of our results under the influence of the tip vortex and blade vortex interactions, they invoked three-dimensional effects and spanwise flow to explain the discrepancy. In both cases, the assumption that 2D airfoil aerodynamics applies is not valid. Actuator methods or AoA extraction techniques are bound to fail in that region unless a proper 3D correction can be developed.

As suggested in (Refs. 23,41), effective AoA extraction methods could help determine 2D polars already corrected for 3D effects directly from 3D simulations instead of relying on ad-hoc corrections. This has the potential to bring results of actuator methods in closer agreement to the state-of-the-art high-fidelity blade-resolved simulations.

Finally, this study did not explore the influence of various geometrical (e.g., grid topology), numerical (e.g., schemes such as RANS versus large eddy simulation), or environmental (e.g., unsteadiness) parameters on the AoA extraction results. One can expect that any change to the circulation distribution of the airfoil will affect the AoA extraction, as could be the case for e.g. turbulence (Ref. 43) or transition modeling (Ref. 40). This remains to be thoroughly quantified and will be the topic of subsequent work.

Author contact: Patricia Ventura Diaz, patricia.ventura-diaz@nasa.gov

REFERENCES

1. Sørensen, J. N., Mikkelsen, R. F., Henningson, D. S., Ivanell, S., Sarmast, S., and Andersen, S. J., "Simulation of wind turbine wakes using the actuator line technique," *Proceedings of the Royal Society of London. Series A, Mathematical and Physical Sciences*, Vol. 373, (2035), 2015. DOI: 10.1098/rsta.2014.0071.

2. Martinez-Tossas, L. A., Churchfield, M. J., and Leonardi, S., "Large eddy simulations of the flow past wind turbines: actuator line and disk modeling," *Wind Energy*, Vol. 18, (6), 2015, pp. 1047–1060.

3. Moens, M., Duponcheel, M., Winckelmans, G., and Chatelain, P., "An actuator disk method with tip-loss correction based on local effective upstream velocities," *Wind Energy*, Vol. 21, (9), 2018, pp. 766–782. DOI: 10.1002/we.2192.

4. van Kuik, G. A. M., "On the velocity at wind turbine and propeller actuator discs," *Wind Energy Science*, Vol. 5, (3), 2020, pp. 855–865. DOI: 10.5194/wes-5-855-2020.

5. Caprace, D.-G., Chatelain, P., and Winckelmans, G., "Lifting Line with Various Mollifications: Theory and Application to an Elliptical Wing," *AIAA Journal*, Vol. 57, (1), 2019, pp. 17–28. DOI: 10.2514/1.J057487.

6. Churchfield, M. J., Schreck, S., Martinez-Tossas, L. A., Meneveau, C., and Spalart, P. R., "An Advanced Actuator Line Method for Wind Energy Applications and Beyond," 35th Wind Energy Symposium, 2017.

7. Merabet, R., and Laurendeau, E., "Parametric Study on the Velocity Sampling Techniques for the Actuator Line Method in 2D," AIAA Scitech 2019 Forum, 2019. DOI: 10.2514/6.2019-1797.

8. Martínez-Tossas, L., Churchfield, M., and Meneveau, C., "Optimal smoothing length scale for actuator line models of wind turbine blades based on Gaussian body force distribution," *Wind Energy*, Vol. 20, 2017, pp. 1083–1096. DOI: 10.1002/we.2081.

9. Caprace, D.-G., Winckelmans, G., and Chatelain, P., "An immersed lifting and dragging line model for the vortex particle-mesh method," *Theoretical and Computational Fluid Dynamics*, Vol. 34, 2020, pp. 21–48. DOI: 10.1007/s00162-019-00510-1.

10. Xie, S., "An actuator-line model with Lagrangian-averaged velocity sampling and piecewise projection for wind turbine simulations," *Wind Energy*, Vol. 24, (10), 2021, pp. 1095–1106. DOI: 10.1002/we.2619.

11. Melani, P. F., Balduzzi, F., Ferrara, G., and Bianchini, A., "Tailoring the actuator line theory to the simulation of Vertical-Axis Wind Turbines," *Energy Conversion and Management*, Vol. 243, 2021, pp. 114422. DOI: 10.1016/j.enconman.2021.114422.

12. Melani, P. F., Mohamed, O. S., Cioni, S., Balduzzi, F., and Bianchini, A., "An insight into the capability of the actuator line method to resolve tip vortices," *Wind Energy Science*, Vol. 9, (3), 2024, pp. 601–622. DOI: 10.5194/wes-9-601-2024.

13. Van Hoydonck, W., Haverdings, H., and Pavel, M., "A review of rotorcraft wake modeling methods for flight dynamics applications," 35th European Rotorcraft Forum, Vol. 58, 2009.

14. Barakos, G., Fitzgibbon, T., Kusyumov, A., Kusyumov, S., and Mikhailov, S., "CFD simulation of helicopter rotor flow based on unsteady actuator disk model," *Chinese Journal of Aeronautics*, Vol. 33, (9), 2020, pp. 2313–2328. DOI: 10.1016/j.cja.2020.03.021.

15. Stich, G.-D., Fernandes, L. S., Duensing, J. C., Housman, J. A., Kenway, G. K., and Kiris, C. C., "Validation of Actuator Disk, Actuator Line and Sliding Mesh Methods within the LAVA Solver," Paper ICCFD11-2022-0903, The 11th International Conference on Computational Fluid Dynamics, 2022.

16. Garcia Perez, D., Ventura Diaz, P., and Yoon, S., "A Comparison of Rotor Disk Modeling and Blade-Resolved CFD Simulations for NASA's Tiltwing Air Taxi," Proceedings of the 79th VFS annual forum, West Palm Beach, FL, May 16–18, 2023.

17. Caprace, D.-G., Chatelain, P., and Winckelmans, G., "Wakes of rotorcraft in advancing flight: A large eddy simulation study," *Physics of Fluids*, Vol. 32, (8), 2020, pp. 087107. DOI: 10.1063/5.0015162.

18. Merabet, R., and Laurendeau, E., "Hovering Helicopter Rotors Modeling Using the Actuator Line Method," *Journal of Aircraft*, Vol. 0, (0), 2021, pp. 1–14. DOI: 10.2514/1.C036314.

19. Stanly, R., Martínez-Tossas, L. A., Frankel, S. H., and Delorme, Y., "Large-Eddy Simulation of a wind turbine using a Filtered Actuator Line Model," *Journal of Wind Engineering and Industrial Aerodynamics*, Vol. 222, 2022, pp. 104868. DOI: https://doi.org/10.1016/j.jweia.2021.104868.

20. Wissink, A. M., Jude, D., Sitaraman, J., and Tran, S., "Application of CREATE-AV Helios to XV-15 Tiltrotor," AIAA SCITECH 2023 Forum, 2023. DOI: 10.2514/6.2023-0418.

21. Johansen, J., and Sørensen, N. N., "Aerofoil characteristics from 3D CFD rotor computations," *Wind Energy*, Vol. 7, (4), 2004, pp. 283–294. DOI: 10.1002/we.127.

22. Guntur, S., and Sørensen, N. N., "An evaluation of several methods of determining the local angle of attack on wind turbine blades," *Journal of Physics: Conference Series*, Vol. 555, (1), dec 2014, pp. 012045. DOI: 10.1088/1742-6596/555/1/012045.

23. Bak, C., Johansen, J., and Andersen, P., "Three-dimensional corrections of airfoil characteristics based on pressure distributions (paper and poster)," Proceedings (online), 2006 European Wind Energy Conference and Exhibition, EWEC 2006 ; Conference date: 27-02-2006 Through 02-03-2006, 2006.

24. Soto-Valle, R., Bartholomay, S., Alber, J., Manolesos, M., Nayeri, C. N., and Paschereit, C. O., "Determination of the angle of attack on a research wind turbine rotor blade using surface pressure measurements," *Wind Energy Science*, Vol. 5, (4), 2020, pp. 1771–1792. DOI: 10.5194/wes-5-1771-2020.

25. Shen, W. Z., Hansen, M. O., and Sørensen, J. N., "Determination of angle of attack (AOA) for rotating blades," Wind Energy: Proceedings of the Euromech Colloquium, 2006.

26. Shen, W. Z., Hansen, M. O. L., and Sørensen, J. N., "Determination of the angle of attack on rotor blades," *Wind Energy*, Vol. 12, (1), 2009, pp. 91–98. DOI: 10.1002/we.277.

27. Jost, E., Klein, L., Leipprand, H., Lutz, T., and Krämer, E., "Extracting the angle of attack on rotor blades from CFD simulations," *Wind Energy*, Vol. 21, (10), 2018, pp. 807–822. DOI: 10.1002/we.2196.

28. Rahimi, H., Hartvelt, M., Peinke, J., and Schepers, J., "Investigation of the current yaw engineering models for simulation of wind turbines in BEM and comparison with CFD and experiment," *Journal of Physics: Conference Series*, Vol. 753, (2), sep 2016, pp. 022016. DOI: 10.1088/1742-6596/753/2/022016.

29. Zhong, W., Shen, W. Z., Wang, T. G., and Zhu, W. J., "A New Method of Determination of the Angle of Attack on Rotating Wind Turbine Blades," *Energies*, Vol. 12, (20), 2019. DOI: 10.3390/en12204012.

30. Rahimi, H., Schepers, J., Shen, W., García, N. R., Schneider, M., Micallef, D., Ferreira, C. S., Jost, E., Klein, L., and Herráez, I., "Evaluation of different methods for determining the angle of attack on wind turbine blades with CFD results under axial inflow conditions," *Renewable Energy*, Vol. 125, 2018, pp. 866–876. DOI: 10.1016/j.renene.2018.03.018.

31. Zilic de Arcos, F., Vogel, C. R., and Willden, R. H. J., "Extracting angles of attack from blade-resolved rotor CFD simulations," *Wind Energy*, Vol. 23, (9), 2020, pp. 1868–1885. DOI: 10.1002/we.2523.

32. Melani, P. F., Balduzzi, F., Ferrara, G., and Bianchini, A., "How to extract the angle attack on airfoils in cycloidal motion from a flow field solved with computational fluid dynamics? Development and verification of a robust computational procedure," *Energy Conversion and Management*, Vol. 223, 2020, pp. 113284. DOI: 10.1016/j.enconman.2020.113284.

33. Mohamed, O. S., Melani, P. F., Balduzzi, F., Ferrara, G., and Bianchini, A., "An insight on the key factors influencing the accuracy of the actuator line method for use in vertical-axis turbines: Limitations and open challenges," *Energy Conversion and Management*, Vol. 270, 2022, pp. 116249. DOI: 10.1016/j.enconman.2022.116249.

34. Lindenburg, C., "Investigation into rotor blade aerodynamics," *ECN, Peten*, 2003.

35. Johnson, W., *CAMRAD II Comprehensive Analytical Model of Rotorcraft Aerodynamics and Dynamics—Theory Manual*, 1993.

36. Du, Z., and Selig, M., "A 3-D stall-delay model for horizontal axis wind turbine performance prediction," 1998 ASME Wind Energy Symposium, 1998. DOI: 10.2514/6.1998-21.

37. Pulliam, T., "High Order Accurate Finite-Difference Methods: as seen in OVERFLOW," Paper AIAA 2011-3851, Proceedings of the 20th AIAA Computational Fluid Dynamics Conference, Honolulu, HI, June 27–30, 2011. DOI: 10.2514/6.2011-3851.

38. Maisel, M. D., *The History of the XV-15 Tilt Rotor Research Aircraft: From Concept to Flight*, Paper 17, National Aeronautics and Space Administration, Office of Policy and Plans, NASA History Division, 2000.

39. Ventura Diaz, P., and Yoon, S., "High-Fidelity Simulations of a Quadrotor Vehicle for Urban Air Mobility," Paper AIAA 2022-0152, Proceedings of the AIAA SCITECH Forum, San Diego, CA, January 3–7, 2022. DOI: 10.2514/6.2022-0152.

40. Garcia Perez, D., Grant, D. J., Sanguinetti, A. J., Caprace, D.-G., Ventura Diaz, P., and Yoon, S., "Effect of Transition Modeling on the XV-15 Hovering Rotor Flows," AIAA Aviation Forum, 2024. DOI: 10.2514/6.2024-4611.

41. Wimshurst, A., and Willden, R. H. J., "Extracting lift and drag polars from blade-resolved computational fluid dynamics for use in actuator line modelling of horizontal axis turbines," *Wind Energy*, Vol. 20, (5), 2017, pp. 815–833. DOI: 10.1002/we.2065.

42. Melani, P. F., Mohamed, O. S., Cioni, S., Balduzzi, F., and Bianchini, A., "Tuning the Actuator Line Method to Properly Modelling Tip Effects in Finite-Length Blades," *Journal of Physics: Conference Series*, Vol. 2767, (5), jun 2024, pp. 052018. DOI: 10.1088/1742-6596/2767/5/052018.

43. Garcia Perez, D., Ventura Diaz, P., and Yoon, S., "High-Fidelity Simulations of a Tiltwing Vehicle for Urban Air Mobility," AIAA SCITECH 2023 Forum, 2023. DOI: 10.2514/6.2023-2282.